A Genetically Encoded Magnetic Resonance Imaging Reporter Enables Sensitive Detection and Tracking of Spontaneous Metastases in Deep Tissues

Nivin N. Nyström[1,2], Sean W. McRae[1,3], Francisco M. Martinez[3], John J. Kelly[3], Timothy J. Scholl[1,3,4,5], and John A. Ronald[1,3,6]

ABSTRACT

Metastasis is the leading cause of cancer-related death. However, it remains a poorly understood aspect of cancer biology, and most preclinical cancer studies do not examine metastasis, focusing solely on the primary tumor. One major factor contributing to this paradox is a gap in available tools for accurate spatiotemporal measurements of metastatic spread *in vivo*. Here, our objective was to develop an imaging reporter system that offers sensitive three-dimensional (3D) detection of cancer cells at high resolutions in live mice. An *organic anion-transporting polypeptide 1b3 (oatp1b3)* was used as an MRI reporter gene, and its sensitivity was systematically optimized for *in vivo* tracking of viable cancer cells in a spontaneous metastasis model. Metastases with *oatp1b3*-MRI could be observed at the single lymph node level and tracked over time as cancer cells spread to multiple lymph nodes and different organ systems in individual animals. While initial single lesions were successfully imaged in parallel via bioluminescence, later metastases were largely obscured by light scatter from the initial node. Importantly, MRI could detect micrometastases in lung tissue comprised on the order of 1,000 cancer cells. In summary, *oatp1b3*-MRI enables longitudinal tracking of cancer cells with combined high resolution and high sensitivity that provides 3D spatial information and the surrounding anatomical context.

Significance: An MRI reporter gene system optimized for tracking metastasis in deep tissues at high resolutions and able to detect spontaneous micrometastases in lungs of mice provides a useful tool for metastasis research.

Introduction

Metastasis is responsible for approximately 90% of cancer-related mortalities, yet this process remains poorly understood (1). Preclinical animal studies provide a valuable platform for investigating metastasis, intermediate to reductionist *in vitro* models and expensive clinical trials (2). Still, approximately 75% of preclinical animal studies published in leading cancer journals do not investigate metastasis to any extent, instead focusing only on the primary tumor, largely due to a lack of methods for accurate spatiotemporal quantification of metastatic burden (3). Spontaneous metastasis models, which recapitulate the entire metastatic cascade and better mimic clinical disease, are even rarer in the literature, as they complicate experiments further with increased variability between animals in both the rate and site pattern of metastatic progression (4).

Bioluminescence imaging (BLI) is routinely used for assessing whole animal burden in experimental metastasis models because of its high throughput and sensitivity; but assessing total burden on BLI with accuracy, especially in spontaneous metastasis models that include primary tumors, remains a challenge. Light scatter from larger lesions and light attenuation by surrounding tissues contribute to poor resolution, signal loss and/or obscurement of smaller or more deep-seated metastases (5). With current imaging methods, lesion size, depth and precise location remain unclear prior to posthumous examination. Preclinical studies have therefore paired BLI with tissue clearing protocols, light-sheet microscopy, and deep-learning methods for sensitive imaging of metastatic cells at endpoint (6–9). Alternate to BLI, other approaches include implantation of permanent optical windows for real-time monitoring of specific tissue sites (10) or reverting to nonmammalian model organisms to accomplish longitudinal, high resolution, *in vivo* imaging of metastasis (11).

MRI uniquely provides high resolution, three-dimensional (3D) spatial information with excellent soft tissue contrast and is extensively used for assessment of primary tumors and metastatic lesions (12, 13). Although MRI offers versatile contrast mechanisms to enhance lesions on images, it still faces challenges in detecting small metastases due to its relatively low sensitivity. Current MRI probes require that lesions grow to diameters of at least 0.5 mm in lungs of mice, and even larger diameters at other tissue sites for reliable detection (14, 15). Reporter genes for MRI have previously been developed to enhance contrast of cells of interest (16–22), but have not been seriously explored for preclinical tracking of metastasis.

For example, *organic anion-transporting polypeptide 1* (*oatp1*), which encodes a 12-transmembrane-domain integral membrane protein, was previously established as a reporter gene based on its ability to bind and transport gadolinium ethoxybenzyl diethylenetriamine pentaacetic acid (Gd-EOB-DTPA) from the extracellular environment into *oatp1*-engineered cells (**Fig. 1A**; ref. 23). Using variable genetic

[1]Department of Medical Biophysics, Western University, London, Ontario, Canada. [2]Department of Chemical Engineering, California Institute of Technology, Pasadena, California. [3]Imaging Laboratories, Robarts Research Institute, Western University, London, Ontario, Canada. [4]Department of Physics and Astronomy, Western University, London, Ontario, Canada. [5]Ontario Institute for Cancer Research, Toronto, Ontario, Canada. [6]Lawson Health Research Institute, London, Ontario, Canada.

T.J. Scholl and J.A. Ronald contributed equally as co-senior authors of this article.

Corresponding Authors: Timothy J. Scholl, Robarts Research Institute, Room 2241B, Schulich School of Medicine and Dentistry, Western University, 1151 Richmond Street, London, ON N6A 5B7, Canada. Phone: 519-931-5777, ext. 20019; E-mail: tscholl@robarts.ca; and John A. Ronald, jronald@robarts.ca

Cancer Res 2023;83:673–85

doi: 10.1158/0008-5472.CAN-22-2770

engineering approaches and imaging parameters (Supplementary Table S1), we and others applied *oatp1*-MRI to *in vivo* cancer imaging of xenografts and orthotopic lesions, and demonstrated its ability to generate high-resolution images of primary tumor architecture (24), but at best observed an *in vivo* detection limit of $\sim 10^6$ cells per lesion (25). Meanwhile, non-MR reporter genes recently achieved detection of single isolated cells on BLI (26) and detection of lesions on the order of 10^4 cells on positron emission tomography (27).

With multiple factors contributing to *oatp1*-MRI performance, from genetic construct design to biophysical imaging parameters, we hypothesized that systematic optimization of the imaging framework could greatly improve its *in vivo* detection limit. Accordingly, our primary objective was to increase the sensitivity of the *oatp1*-MRI system for detection and dynamic tracking of *oatp1*-engineered cancer cells in a spontaneous metastasis model of breast cancer. We report that *oatp1*-MRI produces highly-sensitive, 3D, and high-resolution images of metastatic progression in live mice over time; we improve system sensitivity by two to three orders of magnitude relative to previous studies (23–25), enabling detection of as few as 10^3 cells per lesion in lung tissue. Importantly, *oatp1*-MRI enables detection of reporter gene signals that are unaffected by tissue depth or the presence of adjacent lesions. The information afforded by *oatp1*-MRI thus enables precise determination of lesion size, depth, and location for spatiotemporal profiling of metastatic burden in deep tissues of live animals.

Materials and Methods

Lentivirus production

A lentiviral transfer plasmid co-encoding tdTomato fluorescent protein with firefly luciferase 2 was previously cloned (24). The cDNA for Organic anion transporting polypeptide 1b1 (hOATP1B1/SLCO1B1, NCBI Ref. ID: NP_006437) and 1b3 (hOATP1B3/SLCO1B3, NCBI Ref. ID: NP_062818) were acquired from VersaClone cDNA Vectors (RDC0160 and RDC0870, respectively; R&D Systems) and cloned as previously described (28) into separate lentivirus transfer plasmids each co-encoding zsGreen fluorescent protein (**Fig. 1B**). Third-generation packaging and envelope-expression plasmids, pMDLg/pRRE, pRSV-Rev, and pMD2.G (RRIDs: Addgene_12251, Addgene_12253, Addgene_12259, respectively; these were gifts from Didier Trono) were cotransfected with each of the three transfer plasmids (tdTomato/Luciferase, zsGreen/Oatp1b1, zsGreen/Oatp1b3) into 293T cells using Lipofectamine 3000 according to the manufacturer's lentiviral production protocol (Thermo Fisher Scientific Inc.). Lentivirus-containing supernatants were harvested 24 h and 48 h post-transfection, filtered through a 0.45-μm filter, and used immediately for transductions.

Cell culture and stable cell generation

293T (human embryonic kidney, CRL-3216, RRID: CVCL_0063) and MDA-MB-231 (human triple-negative breast carcinoma, HTB-26, RRID: CVCL_0062) cell lines were obtained from the ATCC and cultured in DMEM supplemented with 10% fetal bovine serum at 37°C and 5% CO_2. Cells were routinely verified as free of *Mycoplasma* using the MycoAlert Mycoplasma Detection Kit (Lonza Group). MDA-MB-231 cells were transduced with lentivirus (multiplicity of infection, MOI = 5) co-encoding tdTomato and firefly luciferase 2, and sorted for tdTomato-positive cells using a FACSAria III cell sorter (BD Biosciences). The cells were then expanded and transduced with lentivirus (MOI = 5) co-encoding zsGreen and Oatp1b1 or Oatp1b3 and FACS was performed to select for double-positive cells. Sorted cells, referred to as either Luc-CTL, Luc-1B1, or Luc-1B3, were used for all subsequent experiments.

In vitro bioluminescence

Cells were seeded into 24-well plates with the following numbers of cells per well: 1×10^6, 5×10^5, 3×10^5, 1×10^5, and 5×10^4. Immediately after seeding, 0.15-mg/mL D-luciferin was added to each well, and plates were imaged on an IVIS Lumina XRMS *In Vivo* Imaging System (PerkinElmer). Average radiance values in p/s/cm^2/sr were measured from each well using Living Image software (PerkinElmer, RRID: SCR_014247).

Western blot

Approximately 1×10^6 Luc-CTL, Luc-1B1, and Luc-1B3 cells were washed 3× in PBS and incubated with 200 μL of chilled RIPA buffer and protease inhibitors for 30 minutes. Lysates were collected and sonicated with five 5-s 40-kHz bursts before being centrifuged at 13,000 g for 20 minutes at 4°C. Supernatants were collected, quantified and 40 μg of protein from each sample was loaded into an acrylamide gel composed of a 4.0% stacking layer buffered at pH 6.8 and a 15% separation layer buffered at pH 8.8. Gel electrophoresis was performed for 20 minutes at 90 V and 1 hour at 110 V. Protein was transferred to a nitrocellulose membrane for 7.5 minutes via the iBlot 2 Gel Transfer Device (IB21001, Thermo Fisher Scientific) and blocked with 0.05% Tween-20, 3% BSA solution for 30 minutes. Rabbit anti-Oatp1b3 antibody (1:1000 dilution, ab139120, Abcam, RRID: AB_2924978) was added and incubated overnight at 4°C. The blot was washed 3× with 0.05% Tween-20 solution for 10 minutes and Goat anti-Rabbit 790-nm antibody (1:10,000 dilution, A11369, Thermo Fisher Scientific, RRID: AB_2534142) was added for 45 minutes at room temperature. The blot was washed again 3× with 0.05% Tween-20 solution for 10 minutes and imaged on the Odyssey CLx Imaging System (LI-COR Biosciences, RRID: SCR_014579).

Transmission electron microscopy

A total of 3×10^5 Luc-1B3 cells were seeded and grown on Thermanox cover slips (150067, Thermo Fisher Scientific) until confluency was reached, after which, cells were incubated with 1 mmol/L Gd-EOB-DTPA or an equivalent volume of saline in DMEM for 1 hour. Following contrast agent incubation, cells were washed 3 × with PBS, and incubated for 10 minutes with a 1:1 solution of Karnovsky's fixative (2% paraformaldehyde, 2.5% glutaraldehyde in 0.1 mol/L cacodylate buffer, pH = 7.4) and DMEM at 37°C, and then subsequently incubated for 3 hours with Karnovsky's fixative at room temperature. Finally, cells were washed 4×, for 5 minutes each time, with 0.1 mol/L cacodylate buffer.

Induced coupled plasma mass spectrometry

3×10^5 Luc-CTL and Luc-1B3 cells ($n = 3$) were seeded in 6-well plates and allowed to grow for approximately three days, until confluency was reached. Cells were then treated with variable concentrations of Gd-EOB-DTPA (0, 1.6, 3.2, 6.4, 9.6, 16.0 mmol/L), washed 3 × with PBS, trypsinized and counted. One million cells of each condition were harvested and lysed via 20-minute shaking incubation with 500 μL of 25 mmol/L Tris•HCl, 150-mmol/L NaCl, 1% NP-40, 1% sodium deoxycholate and 0.1% sodium dodecyl sulfate. The lysate was then digested by adding 10% (v/v) HNO_3 solution to bring the final sample volume to 10 mL.

In vitro nuclear magnetic relaxometry

For all *in vitro* magnetic characterization experiments, 1×10^6 cells were seeded in T-175 cm flasks and allowed to grow for three days. Cells were incubated with Gd-EOB-DTPA or Gd-DTPA at specific concentrations and lengths of time prior to being washed 3× with PBS and collected for imaging. The following parameters were used for each experimental objective:

- For nuclear magnetic relaxation dispersion, cells were incubated with 16 mmol/L Gd-EOB-DTPA or Gd-DTPA for 1 hour. For measurements at 3 T, cells were incubated with either 1.6- or 16-mmol/L Gd-EOB-DTPA or Gd-DTPA for 1 hour.
- To evaluate reporter-probe kinetics, Luc-1B3 cells were incubated with 16-mmol/L Gd-EOB-DTPA for 0, 10, 20, 30, 45, 60, or 90 minutes. In parallel, Luc-CTL cells were incubated with 16-mmol/L Gd-EOB-DTPA and Luc-1B3 cells were incubated with 16-mmol/L Gd-DTPA for 90 minutes as controls.
- To determine volume fraction sensitivity, Luc-CTL and Luc-1B3 cells were incubated separately with 16-mmol/L Gd-EOB-DTPA for 1 hour, counted, and mixed into tubes at the following Luc-CTL to Luc-1B3 ratios: 1:0 (0%), 99:1 (1%), 195:5 (2.5%), 19:1 (5%), 9:1 (10%), 17:1 (15%), 4:1 (20%), 3:1 (25%), 1:1 (50%), and 0:1 (100%).

Following washing, cells were trypsinized, centrifuged and 1×10^7 cells were counted and placed in 300 μL tubes. Nuclear magnetic relaxation dispersion data for the resulting cell pellets were acquired at magnetic fields from 230 μT to 1 T on a fast field-cycling NMR relaxometer (SpinMaster FFC2000 1T C/DC, Stelar, s.r.l.) by changing the relaxation field in 30 steps, logarithmically distributed using an acquisition field of 380.5 mT, all performed at 37°C. Data for each sample were subsequently fit into a LOWESS spline curve.

In vitro MRI was performed on a 3-T GE clinical MR scanner (General Electric Healthcare Discovery MR750 3.0 T) using a clinical 16-channel birdcage RF head coil. A phantom comprised of 1% agarose organized the tubes in a circular pattern to ensure equidistance of all samples to the coil during imaging. Imaging data were acquired at 37°C with a fast spin-echo inversion-recovery (FSE-IR) pulse sequence using the following parameters: matrix size = 256 × 256, repetition time (TR) = 5000 ms, echo time (TE) = 16.4 ms, echo train length (ETL) = 4, number of excitations (NEX) = 1, receiver bandwidth (rBW) = ±12.5 kHz, inversion times (TI) = 20, 35, 50, 100, 125, 150, 175, 200, 250, 350, 500, 750, 1000, 1500, 2000, 2500, 3000, in-plane resolution = 0.2 × 0.2 mm^2, slice thickness = 2.0 mm, acquisition time = 5 min, 25 s per inversion time. Spin-lattice relaxation rates (R_1) were determined by nonlinear least-squares fitting of signal intensities across the series of variable inversion time images on a pixel-by-pixel basis using the following model:

$$S = k\left|M_{ss} - (M_{ss} - M_i)\cdot e^{-TI/T_1}\right|.$$

Here, S represents the acquired signal, and k is the proportionality constant, which depends on the specific coil used, the main magnetic field, the proton density, and the temperature, amongst other factors (29). M_{ss} represents the steady state magnetization, M_i corresponds to the first value of the inversion recovery curve under a non-ideal inversion pulse, and TI is the inversion time. This equation slightly deviates from the standard inversion recovery equation because it takes into account nonperfect 180° RF pulses and the delay between the RF excitation and signal acquisition (30), assuming $TR \gg TI$. The absolute value is used because the stored DICOM images acquired provided only magnitude (non-phase) information. All calculations were performed on MATLAB (MathWorks, RRID: SCR_001622). Source code is available upon request.

Spontaneous metastasis model

Animals were cared for in accordance with the standards of the Canadian Council on Animal Care, and experiments were undertaken with an approved protocol of the University of Western Ontario's Council on Animal Care (AUP 2016–026). Luc-CTL or Luc-1B3 cells (3×10^5) were implanted into the left 4th mammary fat pad of female mice (NOD-*scid* IL2Rγ^{null} strain, NSG, Jackson Laboratory, RRID: BCBC_1262). BLI was performed after 150 mg/kg D-luciferin injection. T_1-weighted 3T-MRI was performed before and 5 h post 1.3 mmol/kg Gd-EOB-DTPA injection. Detectability of widespread metastases was evaluated by imaging Luc-CTL and Luc-1B3 mice ($n = 3$ each) 30 days after cell implantation. A second Luc-1B3 cohort ($n = 7$) was imaged over time until endpoint (Day 22–36, dependent on the overall health of each mouse) to assess dynamic spatiotemporal tracking of metastatic progression.

In vivo BLI

BLI was performed on an IVIS Lumina XRMS *In Vivo* Imaging System (PerkinElmer). Mice were anesthetized with 1–2% isoflurane using a nose cone attached to an activated carbon charcoal filter for passive scavenging and administered 150 μL of 30 mg/mL D-luciferin intraperitoneally. Whole-body BLI was acquired with repeated 1.0 s exposure times every minute for approximately 15 minutes. Once the maximum signal plateaued, the lower half of the mouse i.e., the primary tumor site, was shielded with opaque black cloth and the front limbs of the mice were taped down to fully expose the anterior thoracic region. The field-of-view was adjusted to fit the upper body of the mouse and an image was captured with a 5 minute exposure time. Regions-of-interest (ROI) were manually drawn around primary tumor borders using LivingImage software (PerkinElmer, RRID: SCR_014247) to measure bioluminescent average radiance (p/s/cm^2/sr). For measurements of total metastatic burden in the upper body, rectangular ROIs were drawn according to the perimeter of the mouse thorax, and total photon flux (p/s/) from this region was calculated.

In vivo MRI

Mice ($n = 7$) were anesthetized with 1–2% isoflurane by using a nose cone attached to an activated carbon charcoal filter for passive scavenging and positioned in a lab-built tray that was warmed to 40°C during MRI. All *in vivo* MR imaging used a clinical 3-Tesla GE MR750 clinical scanner (General Electric Healthcare) with a custom-built insert gradient: inner diameter = 17.5 cm, gradient strength = 500 mT/m, peak slew rate = 3,000 T/m/s; and a bespoke 3.5-cm diameter, 5.0-cm length birdcage radiofrequency coil (Morris Instruments). Precontrast T_1-weighted images were acquired using a 3D Fast Spoiled Gradient Recalled Acquisition in Steady State (FSPGR) pulse sequence using the following parameters: frequency field of view (FOV) = 40 mm, slice thickness = 0.2 mm, TR = 14.0 ms, TE = 3.3 ms, matrix size 200×200, rBW = ±31.5 kHz, flip angle = 60°, NEX = 3, voxel size = 200 μm isotropic, scan time = 18–24 minutes per mouse, dependent on mouse size. Volumes of interest (VOI) were manually delineated around metastatic lesions in postcontrast images using open-source code ITK-SNAP (www.itksnap.org, RRID: SCR_002010; ref. 31) and Horos (horosproject.org, Nimble Co LLC d/b/a Purview, RRID:

SCR_017340). VOIs were compared on precontrast and postcontrast images.

Histology

Mice were sacrificed via isoflurane overdose, perfused with 4% paraformaldehyde through the left heart ventricle, and relevant organs were carefully excised. Tissues were frozen in OCT medium (Sakura Finetek) and 10-µm or 150-µm frozen sections were collected onto glass slides. Whole-tissue microscopy images of fluorescence were acquired using an EVOS FL Auto 2 Imaging System (Invitrogen) before hematoxylin and eosin staining of the same and/or adjacent histology sections and subsequent imaging with the same microscope. For whole-mouse imaging, sacrificed mice were submerged in hexane over dry ice for flash freezing, and incubated at −80°C for ≥ 48 hours prior to imaging on the Xerra System (EMIT Imaging) at 60-µm isotropic resolutions.

Statistical analysis

Unless otherwise stated, statistical analysis was performed using Graphpad Prism software (Version 9.00 for Mac OS X; GraphPad Software Inc.; www.graphpad.com, RRID: SCR_002798). Unpaired two-tailed *t* tests, and one or two-way ANOVA and Tukey *post hoc* multiple comparisons were performed, depending on the number of conditions and number of independent variables. For all tests, a nominal *P* value less than 0.05 was considered statistically significant.

Data availability

The data generated in this study are available upon request from the corresponding authors.

Results

In silico and *in vitro* protein characterization of OATP1B3 synthetically expressed in a metastasis-competent cancer cell line

Two lentiviral transfer plasmids, the first encoding *tdTomato fluorescent protein* with *luciferase* and the second plasmid encoding *zsGreen fluorescent protein* with *oatp1b3* were cloned and packaged into lentiviral vectors (**Fig. 1B**). Both transgene cassettes were placed under regulation of the constitutive human elongation factor-1 alpha promoter (pEF1α). A self-cleaving peptide (P2A, T2A, respectively) was used to incorporate fluorescent proteins for FACS and a woodchuck hepatitis virus post-transcriptional regulatory element (WPRE) was used to stabilize mRNA transcript levels. Metastasis-competent human triple-negative breast cancer cells (MDA-MB-231) were transduced with fresh lentivirus and subsequently sorted with gates for high expression (top 3%) of both tdTomato and zsGreen fluorescence

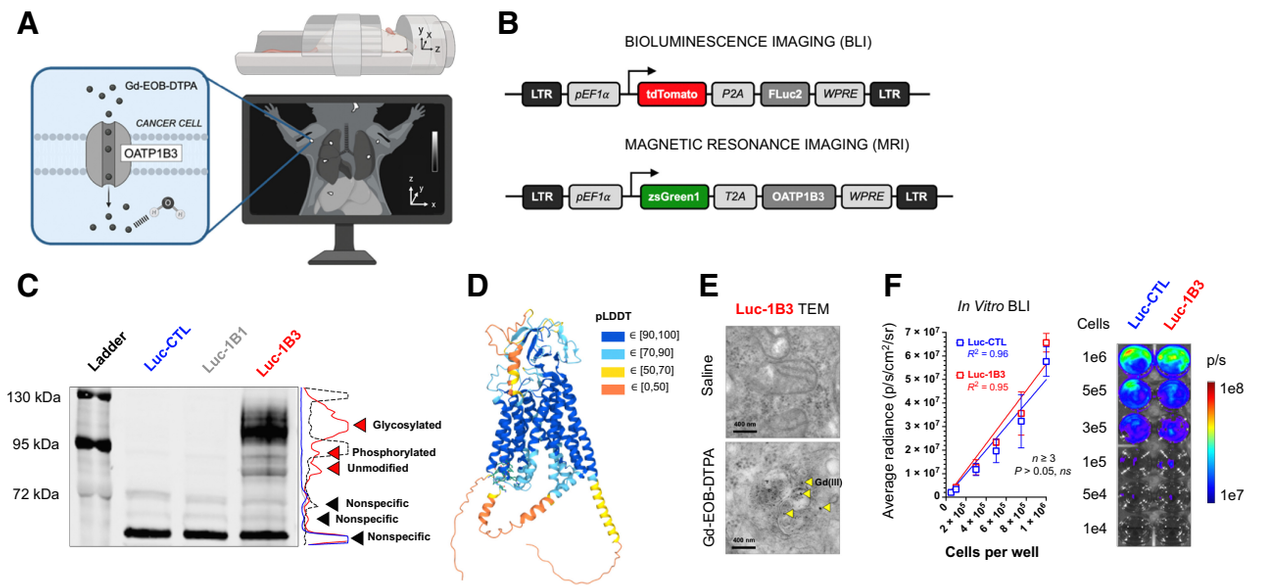

Figure 1.

Principle of *Oatp1b3* as a reporter gene for cancer cell tracking. **A,** Synthetic expression of the OATP1B3 transporter by cancer cells enables Gd-EOB-DTPA uptake into the cellular cytoplasm compartment of cells. This causes increased spin-lattice relaxation of water protons, which can be detected with T_1-weighted MRI producing high-resolution 3D images with anatomical context. **B,** Genetic constructs for transgene expression via lentiviral integration. For BLI, human codon-optimized firefly luciferase (FLuc2) was co-encoded with tdTomato fluorescent protein, which was used as a marker for cell sorting. For MRI, OATP1B3 was co-encoded with zsGreen1 fluorescent protein for cell sorting, long terminal repeat (LTR), human elongation factor-1 alpha promoter, pEF1α, self-cleaving peptides, P2A, T2A, and woodchuck hepatitis virus post-transcriptional regulatory element, WPRE. **C,** Anti-OATP1B3 Western blot of cells engineered with luciferase (Luc-CTL; blue), cells engineered with luciferase and *oatp1b1* (Luc-1B1; gray), and cells engineered with luciferase and *oatp1b3* (Luc-1B3; red). Signal intensity profiles are outlined along position of Western blot. Ladder profile is shown in black. Nonspecific peaks and OATP1B3-specific peaks of unmodified, phosphorylated, and glycosylated OATP1B3 are indicated by arrows. **D,** 3D rendering of AlphaFold prediction for OATP1B3 structure, illustrated with single residue-resolved confidence score. pLDDT, predicted local-distance difference test. **E,** Transmission electron microscopy of Luc-1B3 cells incubated with or without 1-mM Gd-EOB-DTPA for 1 hour. Gd(III) appears as black foci, indicated by yellow arrows. **F,** Average radiance (p/s/cm^2/sr) of increasing numbers of Luc-CTL (blue) and Luc-1B3 cells (red) per well, $n = 3$. $P > 0.05$, ns, nonsignificant. Representative image of well plate. Error bars, SD. (**A**, Created with BioRender.com.)

with > 98% purity to obtain stable *luciferase*-expressing control cells (Luc-CTL), as well as cells with stable coexpression of *luciferase* and *oatp1b3* (Luc-1B3).

Immunoblotting of cell lysates for OATP1B3 protein confirmed its absence in Luc-CTL cells, whereas four peaks at distinct molecular weights, measured at 84 kDa, 92 kDa, 112 kDa, and 120 kDa developed in the Luc-1B3 lane (**Fig. 1C**). Nonspecific bands across all samples were observed at about 60 kDa, 65 kDa, and 72 kDa (**Fig. 1C**). Some posttranslational modifications of OATP1B3 have previously been reported; namely, two glycosylation sites have been associated with its trafficking to the cell membrane and its functionalization (32), whereas increased phosphorylation of OATP1B3 was correlated with downregulation of its transport activity (33). Band analysis with FindMod-ExPASy (expasy.org, Swiss Institute of Bioinformatics; ref. 34) resulted in identification of the 84 kDa band as the unmodified transporter, the band at about 92 kDa as the phosphorylated protein, and the wide band about 112 kDa as the glycosylated transporter with > 95% confidence. Finally, the less intense peak at about 120 kDa was identified as OATP1B3 that is both glycosylated and phosphorylated, albeit with < 95% confidence (35). We outline our post-regulatory site predictions for OATP1B3 in Supplementary Table S2. Importantly, the blot suggests that a significant proportion of the protein synthesized by engineered MDA-MB-231 cells has undergone the glycosylation necessary for functionalization (75.8%, AUC = 40.9 a.u.), whereas a smaller fraction [12.3%, AUC = 6.61 arbitrary units (a.u.)] was phosphorylated but not glycosylated (**Fig. 1C**).

AlphaFold (36) was employed to predict molecular structure of OATP1B3 (Identifier AF-Q9NPD5-F1), generating a model with an overall confidence score (predicted local distance difference test, pLDDT) of 77.6% (**Fig. 1D**; Supplementary Fig. S1). Processing of the OATP1B3 protein sequence and structure (UniProtKB ID SO1B3_HUMAN, UniProtKB Accession Q9NPD5–1), first through iPTMnet (research.bioinformatics.udel.edu/iptmnet/, University of Delaware, Newark, DE; ref. 37), then subsequently via GlyGen (glygen.org, University of Georgia, Athens, GA; ref. 38) and PhosphoSitePlus (phosphosite.org; Cell Signaling Technology; ref. 39) resulted in identification of 8 extracellular N-linked glycosylation sites

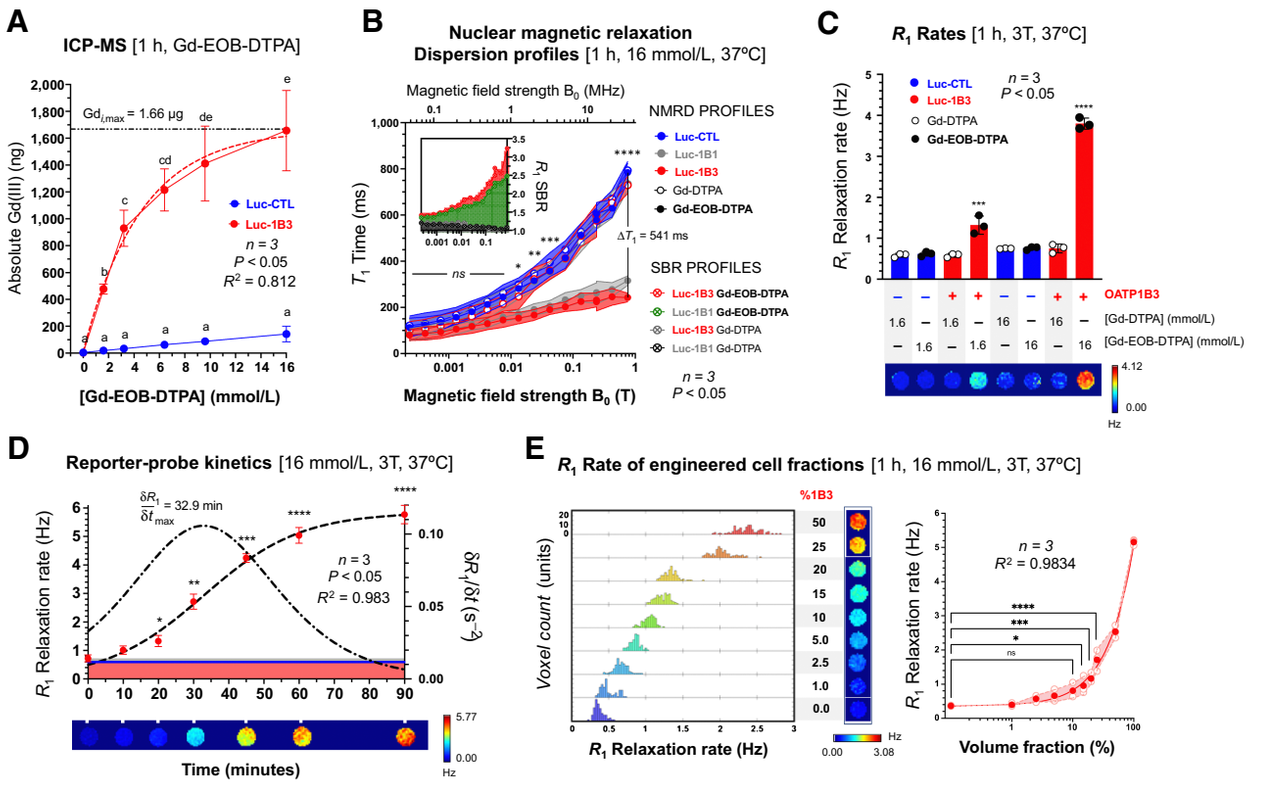

Figure 2.

Characterization of biochemical, magnetic relaxation, and kinetic properties of Gd-EOB-DTPA in a system of mammalian cells expressing *Oatp1b3*. **A,** Inductively coupled plasma mass spectrometry (ICP-MS) of Gd(III) (ng) from lysate of a million Luc-CTL (blue) and Luc-1B3 (red) cells incubated with variable [Gd-EOB-DTPA] for 1 hour, $n = 3$; $R^2 = 0.82$. $Gd_{i,max}$, maximum intracellular Gd(III) mass projected (per million cells). **B,** T_1 time (ms) measured at variable field strength (MHz) of Luc-CTL (blue), Luc-1B1 (gray), and Luc-1B3 (red) cells incubated with either 16 mmol/L Gd-DTPA or Gd-EOB-DTPA for 1 hour. SBR ratio (a.u.) of R_1 relaxation rates of Luc-1B1 (green) and Luc-1B3 (red) cells incubated with Gd-EOB-DTPA is shown in the embedded graph. Background is Luc-CTL cells at the same field strength and probe condition. $n = 3$. **C,** R_1 relaxation rates (Hz) measured at 3 T and 37°C of Luc-CTL (blue) and Luc-1B3 (red) cells incubated with Gd-DTPA or Gd-EOB-DTPA for 1 hour. $n = 3$. **D,** R_1 relaxation rates (Hz) of Luc-1B3 cells at 3 T incubated with 16 mmol/L Gd-EOB-DTPA for variable incubation times at 37°C. $n = 3$. Regression of Luc-1B3 R_1 rates, the first derivative of the regression, Luc-CTL cells incubated with Gd-EOB-DTPA for 90 minutes (blue), Luc-1B3 cells incubated with Gd-DTPA for 90 minutes (pink), and phosphate buffered saline (gray) are also plotted. **E,** R_1 relaxation rates (Hz) of variable Luc-CTL and Luc-1B3 cell ratios at 3 T and 37°C incubated with 16 mmol/L Gd-EOB-DTPA for 1 hour. Red filled circles, average values; pink open circles, individual trial measurements. Shading, SD. $n = 3$; $R^2 = 0.98$. *, $P < 0.05$; **, $P < 0.01$; ***, $P < 0.001$; ****, $P < 0.0001$.

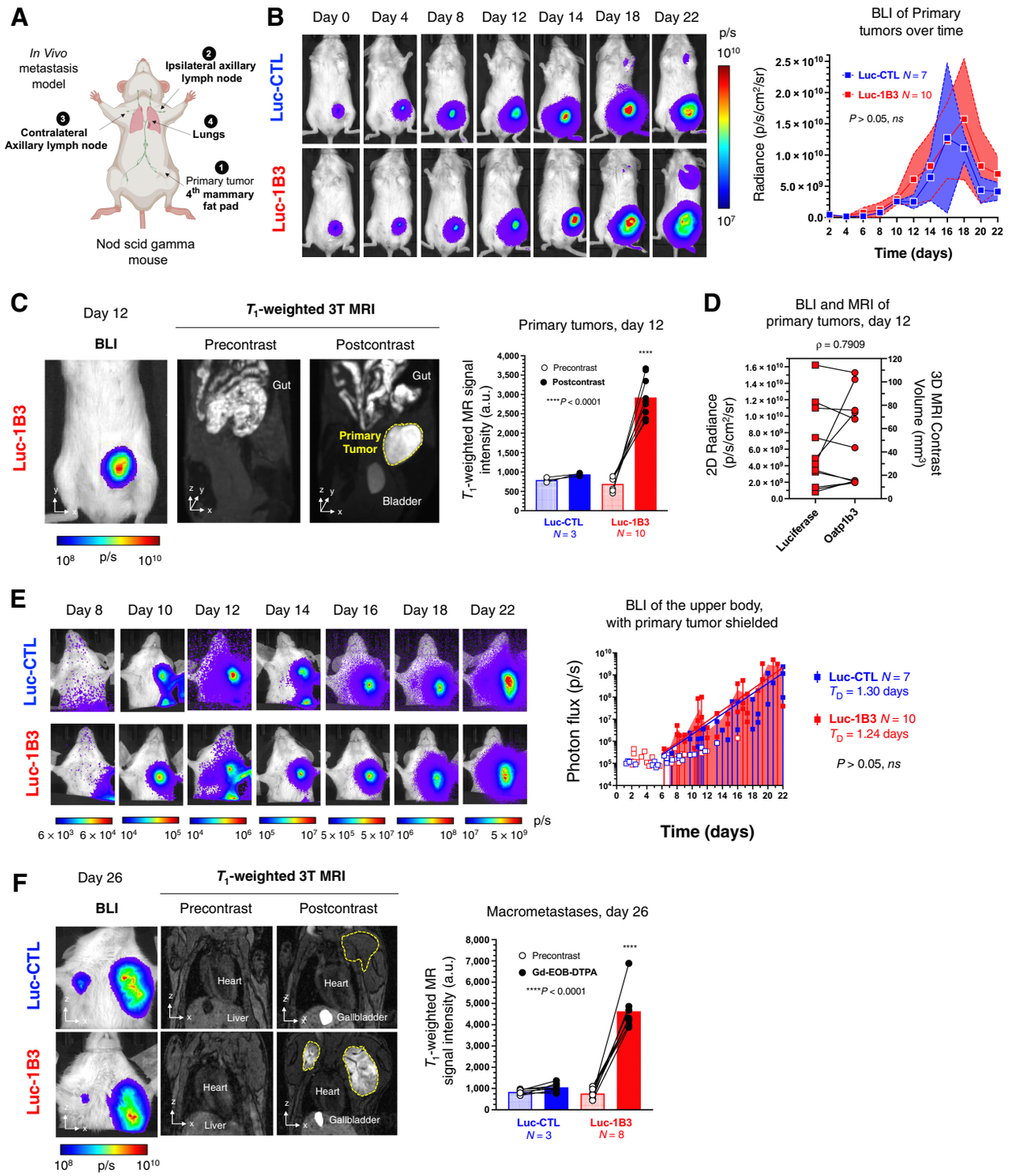

Figure 3.

Deep tissue imaging of primary tumors and metastatic lesions via *Oatp1b3*-MRI. **A,** Spontaneous metastasis model. MDA-MB-231 cells were implanted orthotopically into the left-bearing 4th mammary fat pad of a NSG mouse. Over time, the cells metastasize to the ipsilateral axillary lymph node, to the contralateral axillary lymph node, and to the lungs. **B,** Radiance (p/s/cm^2/sr) from Luc-CTL ($N = 7$; blue) and Luc-1B3 primary tumors ($N = 10$; red) over time. $P > 0.05$, ns, nonsignificant. **C,** Same day BLI. Pre- and postcontrast T_1-weighted MR images of representative Luc-1B3 mouse 12 days post cell implantation at the primary tumor site. Contrast enhancement of primary tumor is outlined in yellow. Average T_1-weighted signal intensity (a.u.) of Luc-CTL ($N = 3$; blue) and Luc-1B3 ($N = 10$; red) primary tumors before and after Gd-EOB-DTPA administration. (*Continued on the following page.*)

and 3 intracellular phosphoserine sites, as well as an intracellular serine protease inhibitor motif characterized by 3 disulfide bonds (Supplementary Table S2).

Transmission electron microscopy of Luc-1B3 cells incubated with Gd-EOB-DTPA confirmed the influx of Gd(III) into the cytoplasmic space of Luc-1B3 cells, where the paramagnetic center would be free to interact with protons of the intracellular environment (**Fig. 1E**). Curiously, Gd(III) was also found encapsulated within residual bodies, destined for exocytosis, suggesting a distinct elimination pathway that to our knowledge has not previously been reported (Supplementary Fig. S2). Finally, BLI demonstrated a strong positive linear correlation between cell number and average radiance (p/s/cm^2/sr) for both Luc-CTL ($R^2 = 0.96$) and Luc-1B3 ($R^2 = 0.95$) cells *in vitro*. The slope of the linear regression was not significantly different between Luc-CTL (55.2 ± 8.1 p/s/cm^2/sr/cell) and Luc-1B3 cells (62.5 ± 1.9 p/s/cm^2/sr/cell; $P = 0.22$; **Fig. 1F**). This serves as an important control for BLI in later animal experiments.

Solving for optimal parameters of imaging for *oatp1b3*-MRI

After cell engineering, we first set out to characterize the biochemical, kinetic, and magnetic relaxation properties of the *oatp1b3* reporter gene system *in vitro* (**Fig. 2**). First, Gd-EOB-DTPA uptake in Luc-CTL and Luc-1B3 cells was measured as a function of applied concentration via inductively coupled plasma mass spectrometry (**Fig. 2A**). A significant increase in intracellular Gd(III) was observed in Luc-1B3 cells at all applied concentrations relative to Luc-CTL cells ($P < 0.05$, $n = 3$), but no significant difference was observed between Luc-CTL cells treated with increasing Gd-EOB-DTPA concentrations ($P > 0.05$, $n = 3$), suggesting that Gd-EOB-DTPA is highly specific to *oatp1b3* and its uptake by non *oatp1b3*-expressing cells is negligible within this timeframe (**Fig. 2A**). After fitting the data to an exponential plateau model ($R^2 = 0.81$), the maximum intracellular capacity of Gd(III) for our system was calculated to be 1.66 μg Gd(III) per million cells, or approximately 1.66 pg Gd(III) per single cell (**Fig. 2A**), which signified that channel-mediated transport of Gd-EOB-DTPA into cells constitutively expressing *oatp1b3* approaches saturation (99.6 ± 18.0% of maximum capacity) at 16 mmol/L Gd-EOB-DTPA.

Although the relaxivity of Gd(III)-based contrast agents, including Gd-EOB-DTPA, decreases as a function of field strength and therefore exhibits its greatest effects at low field ($B_0 < 0.05$ T; Supplementary Fig. S3), tissue R_1 values also decrease along the same axis, and these competing phenomena both affect the resultant contrast enhancement that is central to our endeavor of detecting metastasis *in vivo* with high sensitivity. As expected of nonengineered tissues, with increasing field strength, where $B_0 \in (0.000233, 1.0009)$ T, we observed significant increases in the T_1 times of all cells treated with the control Gd-DTPA probe (7.29-fold; $P < 0.0001$) and Luc-CTL cells treated with the *oatp1b3*-targeted Gd-EOB-DTPA (6.94-fold; $P < 0.0001$; **Fig. 2B**). For Luc-1B3 cells incubated with Gd-EOB-DTPA, Gd(III) becomes a major contributing factor to spin-lattice relaxation time; the T_1 time still increased as a function of field strength (3.04-fold) but was significantly lower than that of control samples ($n = 3$, $P < 0.0001$; **Fig. 2B**). Notably, the difference in T_1 time between Luc-CTL and Luc-1B3 cells both treated with Gd-EOB-DTPA significantly increased with magnetic field strength ($n = 3$; $P < 0.05$; **Fig. 2B**). At the lower field limit of 0.000233 T, ΔT_1 between Luc-CTL and Luc-1B3 cells was 33.1 ± 4.0 ms but this difference increased to 541 ± 20 ms at the upper field limit of 1.0009 T ($n = 3$; $P < 0.0001$; **Fig. 2B**).

At a field strength of 3 T, Luc-1B3 cells incubated with low (1.6 mmol/L) and high (16 mmol/L) Gd-EOB-DTPA concentrations exhibited significantly increased R_1 rates (1.32 ± 0.22, 3.80 ± 0.14 s^{-1}, respectively) compared with all other control conditions ($n = 3$; $P \leq 0.0001$; **Fig. 2C**). Specifically, Luc-1B3 cells exhibited a 2.14 R_1 signal-to-background ratio (SBR) at 1.6 mmol/L Gd-EOB-DTPA concentrations and a more substantial 5.02-fold R_1 SBR at 16 mmol/L Gd-EOB-DTPA concentrations (**Fig. 2C**), which was also greater than the SBR measured at lower fields ($SBR_{1T} = 3.23$; **Fig. 2B**). At fields greater than 3 T, however, Gd-EOB-DTPA relaxivity continues to decrease (Supplementary Fig. S3) while spin-lattice relaxation rates for all tissues become similar as they approach zero, resulting in the marked reduction of contrast enhancement typically observed in high field MRI (i.e., 7 T, 9.4 T; refs. 40, 41). We therefore reasoned that imaging animals at mid-field (i.e., 3 T) would optimize SBR for *in vivo* detection of metastases. All the while, to maximize detection sensitivity while mitigating any toxicity concerns from using concentrations of Gd-EOB-DTPA higher than 16 mmol/L, which would result in only incremental increases to SBR (**Fig. 2A**), we selected an applied concentration of 16 mmol/L Gd-EOB-DTPA for all *in vitro* MRI experiments, and a dose of 1.3 mmol/kg Gd-EOB-DTPA for *in vivo* MRI experiments.

When Luc-1B3 cells were incubated with Gd-EOB-DTPA for variable lengths of time, significant increases in R_1 relative to Luc-CTL cells were first observed at the 20-minute time point (1.33 ± 0.20 Hz; $n = 3$, $P = 0.0015$; **Fig. 2D**). The R_1 of Luc-1B3 cells as a function of Gd-EOB-DTPA treatment time was fit into a logistic growth curve ($R^2 = 0.98$). Its slope reached a maximum at 32.9 minutes, after which, uptake began to decrease (**Fig. 2D**). No significant difference was observed between R_1 at the 60-minute (5.03 ± 0.28 Hz) and 90-minute time points (5.67 ± 0.32 Hz; $n = 3$, $P = 0.053$) as the first derivative approaches zero, suggesting that the intracellular Gd(III) concentration detected via magnetic resonance approaches a steady state ($R_{1,max} = 5.85$ Hz) at about 90 minutes of incubation (96.9 ± 5.5% of $R_{1,max}$; **Fig. 2D**). The slow uptake kinetics observed here as well as the slow cellular efflux of the probe (Supplementary Fig. S4) reinforces the approach of previous work using *oatp1a1*, wherein SBR in mice reached a maximum at approximately 5 h post Gd-EOB-DTPA administration (23, 25).

Next, Luc-CTL and Luc-1B3 cells treated with Gd-EOB-DTPA were combined at various cell number ratios and their spin-lattice relaxation rates were measured at 3T. Relative to a pure sample of Luc-CTL cells (i.e., 0% Luc-1B3; 0.365 ± 0.013 Hz), the minimal volume fraction of Luc-1B3 cells required for a significant increase in R_1 relaxation rate was 15% (0.96 ± 0.26 Hz; $n = 3$, $P = 0.017$; **Fig. 2E**). A strong positive linear correlation between R_1 relaxation rate and Luc-1B3 percent

(*Continued.*) **D,** 2D radiance (p/s/cm^2/sr) and corresponding contrast-enhanced 3D volume (mm^3) of individual Luc-1B3 tumors 12 days post cell implantation, $n = 10$. Spearman rank coefficient, $\rho = 0.79$; ***, $P = 0.0085$. **E,** Photon flux (p/s) measurements from the upper body of Luc-CTL ($N = 7$; blue) and Luc-1B3 ($N = 10$; red) mice over time. Hollow symbols represent signals from BLI with no discernible metastatic foci, whereas filled symbols represent photon flux measurements during times where at least one lesion was detected. T_D, doubling time. $P > 0.05$, ns. **F,** BLI, pre- and postcontrast T_1-weighted images of the upper body of representative Luc-CTL and Luc-1B3 mice 26 days post cell implantation at the primary tumor site. Average T_1-weighted signal intensity (a.u.) of Luc-CTL ($N = 3$; blue) and Luc-1B3 ($N = 8$; red) macrometastatic lesions before and after Gd-EOB-DTPA administration. ****, $P < 0.0001$. (**A**, Created with BioRender.com.)

fraction was observed ($n = 3$, $R^2 = 0.98$; **Fig. 2E**). In combination with the R_1 SBR ratios measured above, the results of these fractional 1B3 volume studies supported the feasibility of sensitive detection of engineered cell populations in animals at high resolution.

Oatp1b3 does not affect overall metastatic burden in mice and significantly enhances visualization of primary tumors and metastatic lesions *in vivo*

Using the results from the *in vitro* characterization experiments, we optimized our MRI parameters for *in vivo* longitudinal imaging of a spontaneous metastasis model of breast cancer in mice (**Fig. 3**). In this model, as the primary tumor grows, metastatic lesions were expected to form across multiple lymph nodes and the lungs, as observed by endpoint histology in previous literature (**Fig. 3A**; ref. 42). It is worth noting that the temporal pattern of spread was not yet established prior to our study, but that the chronology reflected in **Fig. 3A** is evidenced by longitudinal *oatp1b3*-MRI data presented in later figures. NOD/SCID gamma (NSG) mice were implanted with 3×10^5 Luc-CTL ($N = 7$) or Luc-1B3 ($N = 11$) MDA-MB-231 cells at the left 4th mammary fat pad and imaged via BLI (150 mg/kg D-luciferin) every 2 days, and pre- and post-contrast T_1-weighted MRI at 3 T (1.3 mmol/kg Gd-EOB-DTPA) were acquired on day 12 for the primary tumor and day 26 for the upper body. Complete details on MRI parameters can be found in Materials and Methods.

We first wanted to assess whether the *oatp1b3* reporter gene system interfered with primary tumor growth or metastatic progression. BLI demonstrated that primary tumors grew in both Luc-CTL ($N = 7$) and Luc-1B3 ($N = 10$) burdened mice, with no significant difference ($P > 0.42$) in bioluminescent average radiance (p/s/cm^2/sr) at each time-point between the groups (**Fig. 3B**). As primary tumors grew, BLI for metastatic lesions was performed by blocking light from the lower body to enable detection of smaller populations of engineered cells that may have metastasized to the upper body. No significant difference was observed in upper body photon flux (p/s) over time between Luc-CTL ($N = 7$) and Luc-1B3 ($N = 10$) mouse groups ($P = 0.18$; **Fig. 3E**), suggesting that *oatp1b3* reporter gene expression neither inhibited nor promoted metastasis. The doubling time of metastasis in the upper body for Luc-CTL mice was determined to be 1.30 ± 0.53 days compared with 1.24 ± 0.59 days for Luc-1B3 mice ($P = 0.83$; **Fig. 3E**).

On day 12, precontrast and postcontrast T_1-weighted MRI at 3 T exhibited an average 4.2-fold significant increase in signal intensity in Luc-1B3 primary tumors ($P < 0.0001$; **Fig. 3C**), whereas Luc-CTL primary tumors showed no difference between pre- and postcontrast images (1.2-fold, $P > 0.96$; Supplementary Fig. S5). There was a strong positive correlation between 2D radiance measurements from BLI and 3D contrast enhancement volumes generated via *oatp1b3*-MRI, with a Spearman rank-order correlation coefficient (ρ) of 0.791 ($n = 9$, $P = 0.0085$; **Fig. 3D**) and a linear regression correlation coefficient (R^2) of 0.56 ($n = 9$, $P = 0.0055$; Supplementary Fig. S6). However, it is worth noting that the two systems were not absolutely correlated on day 12, even when necrosis was not yet a factor, as indicated by the homogeneity of contrast enhancement across all tumors on MRI (**Fig. 3D**). On day 26, large contrast-enhanced metastatic lesions in the upper body were observed in Luc-1B3 mice post contrast ($N = 8$), but not in Luc-CTL mice ($N = 3$) following administration of Gd-EOB-DTPA (**Fig. 3F**). Interestingly, the postcontrast signal intensity of the metastatic masses on day 26 ($4{,}630 \pm 970$ a.u.) was significantly greater than that of the pre-necrotic primary tumor volume on day 12 ($2{,}930 \pm 510$ a.u.; $P < 0.0001$; **Fig. 3F**).

Imaging of spontaneous metastasis in single animals over time via *oatp1b3*-MRI reveals that BLI largely obscures detection of small, late-stage, and/or deep-seated lesions in mice

With the finding that the *oatp1b3* reporter gene system did not disable or promote metastatic progression, as evidenced on BLI, and the auxiliary finding of greater contrast enhancement from metastatic masses compared with their concomitant primary tumors, we then explored the system's capability of longitudinally imaging the metastatic cascade via *oatp1b3*-MRI with a second cohort of mice ($N = 7$; **Fig. 4**). We wanted to determine the first time point at which metastatic lesions were detectable with either BLI or MRI. Mice were imaged according to the algorithm outlined in Supplementary Fig. S7. Most mice were imaged up to day 22, but smaller subsets were imaged at time points beyond day 22, including day 26 ($N = 3$), day 30 ($N = 3$), and day 36 ($N = 3$), the endpoint of which was determined by the health of each individual mouse. For 5 of the 7 mice, metastatic lesions in the ipsilateral axillary lymph node were detected on MRI at the same time point as BLI (**Fig. 4A**) whereas two mice exhibited signals on MRI at this site up to 48 hours prior to BLI signal being detected (Supplementary Fig. S8). Significantly increased MR signal intensity ($2{,}900 \pm 620$ a.u.) was exhibited relative to surrounding muscle tissue ($1{,}120 \pm 110$ a.u.; SBR = 2.59) at the time of detection ($n = 7$, $P < 0.0001$; **Fig. 4B**). On average, spontaneous metastases were first detected 11.2 ± 1.3 days post primary tumor implantation via *luciferase*-BLI, and 10.2 ± 0.8 days via *oatp1b3*-MRI ($n = 7$, $P > 0.05$, ns).

The most frequently observed spatiotemporal pattern of metastasis was continued growth of the initial metastatic lesion at the ipsilateral axillary lymph node, which was observed with both *luciferase*-BLI and *oatp1b3*-MRI (**Fig. 4C**). By day 22, all mice exhibited a significant increase in signal intensity on T_1-weighted images at the contralateral axillary lymph node ($2{,}650 \pm 790$ a.u.; SBR = 2.44). These contralateral lesions could not be resolved on BLI until day 25.4 ± 1.3 due to light scatter from the first metastatic lesion on the opposite side of the animal ($\Delta x_{avg} = 1.14 \pm 0.08$ cm; **Fig. 4D**). Following this, *oatp1b3*-MRI revealed that 6 of the 7 animals developed numerous micrometastatic lesions (< 1 mm^3) in the lungs (**Fig. 4E**). Again, these lung lesions were small and proximal to the larger lymph node lesions, thereby preventing their detection with BLI (**Fig. 4E**).

Beyond this typical progression, there was marked divergence in spatiotemporal patterns of metastasis between mice, even at early time points. Direct-to-lung metastasis was observed in one mouse on day 10, as both the signal intensity and volume of the lesion in the lung ($SI = 3{,}460 \pm 260$ a.u., $V = 0.067$ mm^3) was already greater than that of its ipsilateral axillary lymph node lesion ($SI = 2{,}510 \pm 120$ a.u., $V = 0.015$ mm^3; **Fig. 4F**); because of the lesion's location behind the heart, as indicated by T_1-weighted images, BLI signals presented as diffuse and relatively imprecise (**Fig. 4F**). In another case, a metastatic lesion in the contralateral kidney was detected via *oatp1b3*-MRI on day 10 ($SI = 5{,}670 \pm 320$ a.u., $V = 0.071$ mm^3, d = 1.39 cm, SBR = 2.84; **Fig. 4G**), but was not detected on BLI due to confounding signals stemming from the primary tumor ($\Delta x = 1.66$ cm). Two additional mice exhibited metastasis to the kidneys on MRI at later dates, which again, could not be resolved on BLI.

On day 22, a minority of mice (3/7) exhibited continued spread through the lymphatic system to the ipsilateral brachial node on T_1-weighted images, but this was virtually impossible to detect on BLI due to the proximity of the node (5.9 mm in one representative mouse) to the initial metastatic lesion (**Fig. 4H**). In one mouse, liver metastases ($V_{total} = 0.18$ mm^3) appeared and outpaced its lung

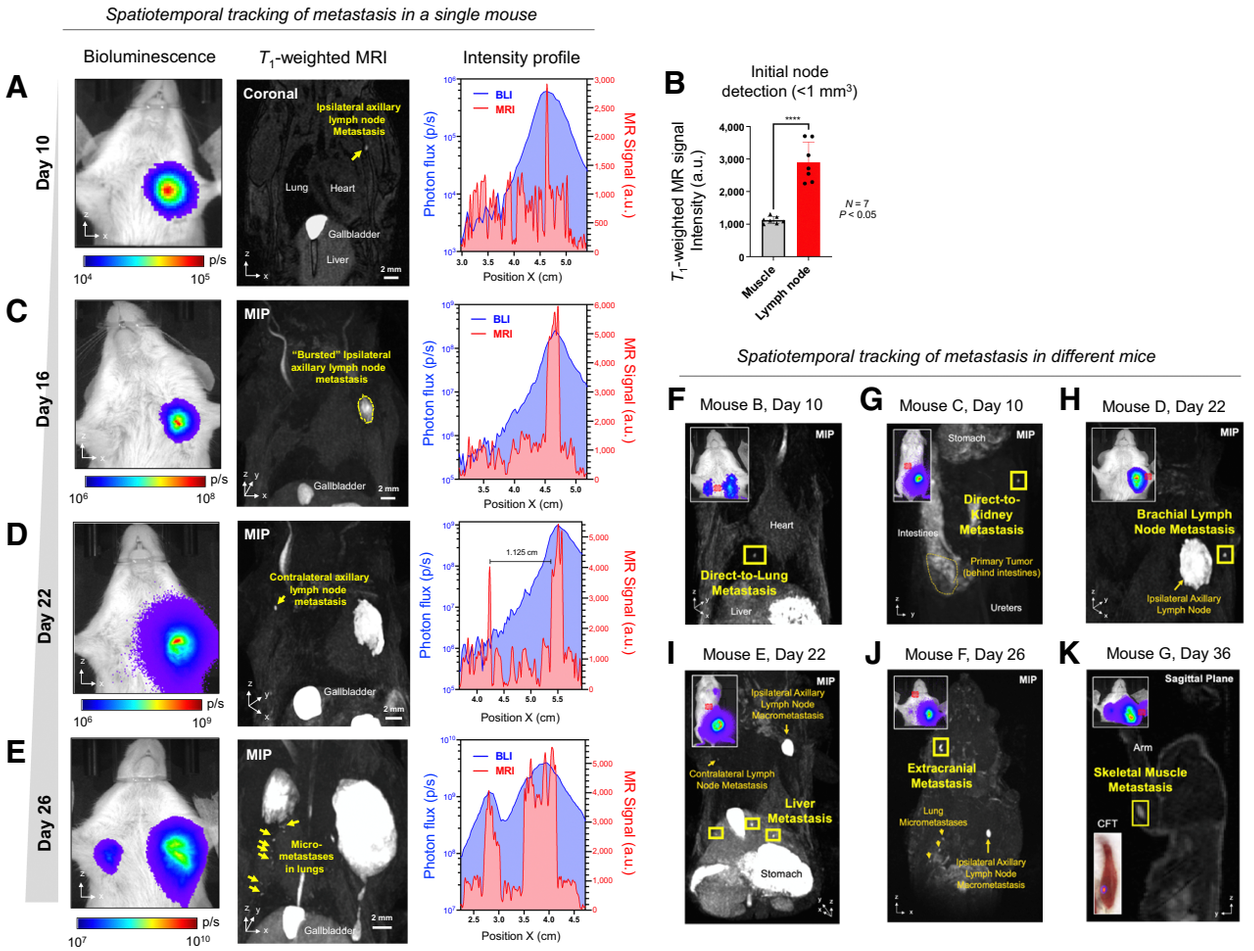

Figure 4.

High resolution, 3D tracking of spontaneous metastasis over time. **A,** and **C–E,** Representative BLIs (p/s), postcontrast T_1-weighted MRI, and line profiles of BLI photon flux (p/s; blue) and MRI signal intensity (a.u.; red) at 3 T of one female NSG mice ($n = 7$) after implantation of MDA-MB-231 cells into the left-bearing 4th mammary fat pad on Day 10 (**A**), Day 16 (**C**), Day 22 (**D**), and Day 26 (**E**). Mouse depicted in **A** is same mouse as in **Fig. 3E** (Day 10, Luc-1B3). Scale bar, 2 mm. **B,** T_1-weighted signal intensity (a.u.) at initial detection of ipsilateral axillary lymph node lesions (Days 10–12) and mean signal intensity (a.u.) of surrounding muscle tissue at 3 T ($n = 7$). ****, $P < 0.0001$. **F–K,** Representative BLI and postcontrast T_1-weighted MR images of unique patterns of metastasis across different mice on different days. Red square on BLI images indicates location of lesion determined by corresponding *oatp1b3*-MRI data. MIP, maximum intensity projection. CFT, cryo-fluorescence tomography.

metastases ($V_{total} = 0.025$ mm^3; **Fig. 4I**). In another case, an extracranial metastasis in the head was detected via *oatp1b3*-MRI, but was obscured on BLI, likely due to the depth of the lesion ($d = 5.6$ mm, $V = 0.15$ mm^3), relative to the larger, more superficial lymph node metastasis ($d = 1.8$ mm, $V = 0.68$ mm^3), in combination with its cavitation between bones in the head, as indicated by T_1-weighted images (**Fig. 4J**). Finally, one mouse also exhibited metastasis to skeletal muscle (4,920 ± 970 a.u., 0.43 mm^3, SBR = 3.9) within its ipsilateral front leg, which was again undetected on BLI due to its proximity to the initial lesion at the ipsilateral axillary lymph node (**Fig. 4K**).

Oatp1b3-MRI enables detection of metastatic lesions comprising as few as 10^3 cells on high resolution, three-dimensional images of live mice

We attempted ($n = 1$) to match micrometastases in the lungs detected on MRI to corresponding lesions on whole-mouse histology generated via the Xerra imaging system (EMIT Imaging). Coordinates were conserved between the two 3D datasets in some localized regions (**Fig. 5A**), but the lack of structural reinforcement in the lungs led to considerable architectural deformation during histologic processing, such that matching lesions from MR images to their precise locations on histology proved challenging without nonrigid image registration that would disturb image integrity considerably. Instead, to acquire an independent estimate of our cellular detection limit, mice imaged on day 30 were immediately sacrificed and the number of cells per micrometastatic lesion in lung tissue was extrapolated from section microscopy (**Fig. 5B–E**).

An analysis of mean signal intensity and volume of individual metastatic foci demonstrated that, for 3 mice, 60 micrometastatic lesions with significantly higher MRI signal than lung background were present in the lungs at about 30 days post cell implantation (**Fig. 5B** and **C**). None of these lesions were detectable with BLI. Metastases as small as a single 200-μm isotropic imaging voxel

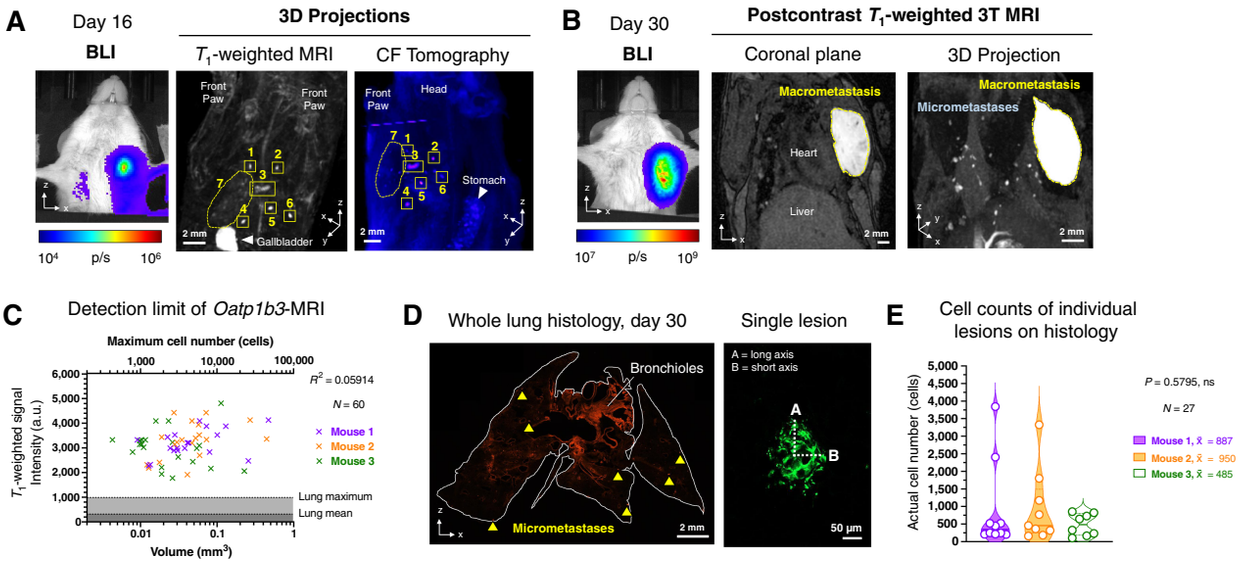

Figure 5.

Ultrasensitive detection of micrometastases in live animals. **A,** BLI (p/s), raw 3D projection of postcontrast T_1-weighted MRI, and raw 3D projection of cryo-fluorescence tomography (CFT) of a Luc-1B3 mouse burdened with lung micrometastases that was imaged and sacrificed 16 days post implantation of its primary tumor. Numbered squares on projections indicated matched MR to CFT lesions. Scale bar, 2 mm. **B,** BLI (p/s), postcontrast T_1-weighted 3 T image, and maximum intensity projection of representative Luc-1B3 mouse on day 30 burdened with a unilateral macrometastatic lesion and numerous micrometastatic lesions across the lungs. Scale bar, 2 mm. **C,** T_1-weighted signal intensity (a.u.) and volume (mm^3) of individual micrometastatic foci ($N = 60$) across Luc-1B3 mice on day 30. $n = 3$; $R^2 = 0.059$. **D,** Representative whole-lung histologic section of Luc-1B3 mouse shown in **A**, imaged via fluorescence for detection of engineered cells. Yellow arrows, metastatic cell populations. Scale bar, 2 mm. Note that bronchioles exhibited autofluorescence. Representative high magnification image of single metastatic lesion. Scale bar, 50 µm. **E,** Cell counts from individual lesions on histology ($N = 27$). Mean cell number per lesion, $\bar{x}$. $P > 0.05$, ns, nonsignificant.

($\sim$0.01 mm^3) were reliably detected above the mean lung signal intensity (**Fig. 5B**). For an epithelial tumor cell line, literature values equate a volume of 1 cm^3 to approximately 10^8 cells (43). Back-calculating from this conversion, 0.01 mm^3 would equate to approximately 10^3 cells per lesion assuming that these voxels were comprised entirely of Luc-1B3 cells. However, it is also worth noting that the range of signal intensities across these foci ($1{,}778 \leq SI \leq 4{,}813$ a.u.) did not correlate with lesion size ($R^2 = 0.059$, $P = 0.13$), suggesting that many of these micrometastatic volumes may not have been comprised entirely of Luc-1B3 cells, and that a detection of limit of 10^3 cells is possibly a conservative estimate. *Ex vivo* microscopy measurements of metastatic lesions supported our *in vivo* calculations, as well as the hypothesis that the *oatp1b3*-MRI system can detect populations comprising as few as 10^3 cells in lung tissue. Five lesions across three mice comprised of greater than 10^3 cells, with the largest measured at an estimated 3,840 cells, but all remaining lesions fell below this threshold. Overall, on average, micrometastases in lung tissue on day 30 were estimated to be comprised of 800 $\pm$ 200 cells ($n = 3$ mice, $N = 27$ lesions).

Discussion

Tracking spatiotemporal patterns of metastatic spread in deep tissues of single animals is an important experimental capability for cancer research. Yet, sensitive and quantitative preclinical assessment of metastatic disease with a high degree of accuracy remains a significant challenge. Compared with traditional contrast agents, reporter genes offer information on cell viability, and do not require the presence of biomarkers to be specific to the cells of interest, as is needed to study triple-negative breast cancer and many other cancer subtypes. To overcome the intensiveness and sampling bias of traditional histology, the last decade has seen a surge of tissue clearing methods that render large biological samples transparent and allow 3D views of large tissue volumes (44). Still, a major drawback of this approach, as with histology, is that only a single time point can be acquired of an individual animal, which in turn, necessitates processing of large numbers of animals to draw meaningful conclusions (45). This is an especially notable issue when working with spontaneous metastasis models that exhibit high variability between animals with respect to both the frequency and location of metastasis (46).

BLI avoids single time point limitations by providing sensitive whole-body information on relative locations of cancer cells in live mice, but we demonstrate that smaller cell populations largely go undetected due to the presence of larger lesions. Specifically, we show that small, single lesions positioned at distances > 1 cm from larger engineered cell populations go undetected unless they grow to substantial sizes before endpoint, and that populations of micrometastases in separate organs remain obscured throughout the BLI timeline (**Fig. 4**). In summary, BLI observations are skewed towards initial, superficial lesions, that may not necessarily progress and respond to treatment in the same way as smaller, late-stage, and/or deep-seated metastases located in distinct microenvironments (47). In fact, promotion of metastasis by antitumor therapies has been previously demonstrated in several major studies (48–50). And on the opposite end, it may be that successful treatments for metastasis have been wrongly deemed ineffective simply because larger lesions

dominated measurements (51). These and other complications contribute to the difficulties in discovering antimetastatic therapies at the preclinical stage as the threshold of metastatic prevention and/or regression is extremely challenging to demonstrate with currently available technologies (52, 53).

Oatp1b3-MRI overcomes many limitations for accurate spatiotemporal tracking of metastatic spread *in vivo*. We show that this system can dynamically track the metastatic process in its earliest stages, at small lymph node lesions, even prior to BLI detection in some cases. At late stages, we demonstrate its superiority over BLI to track cancer spread to multiple lymph nodes and other deep-seated organs on highly resolved images, owing to the inherent absence of signal scatter and signal attenuation in MRI (**Fig. 4**). In parallel, *oatp1b3*-MRI enabled detection of metastatic lesions with high sensitivity, exhibiting an *in vivo* threshold on the order of 10^3 cells per lesion in the lungs (**Fig. 5**). Although the sites of metastasis in this study are in close agreement with previously published literature (42), and a pattern of metastasis similar to that observed in human breast cancer patients is exhibited (54), detailed tracking of metastatic spread in single animals from one location to the next has not previously been demonstrated. Critically, imaging mice at multiple time points with *oatp1b3*-MRI did not result in differences in metastatic spread relative to control mice, making it suitable for noninvasive assessment of antimetastatic therapies in future studies.

Nonetheless, the *oatp1b3*-MRI system is itself not without limitations. The chelated Gd(III) probe used in the system has been subjected to scrutiny in the clinical setting due to findings of long-term retention in human patients following multiple doses of contrast agent over months or years (55). Whether Gd(III) specifically elicits cellular injury within these depositions remains controversial, as no histologic differences were observed between contrast and control groups in a major study that investigated patient tissues posthumously (56). In our own work, it should be noted that we administered relatively large doses of Gd-EOB-DTPA (1.3 mmol/kg) multiple times to individual mice throughout the experimental time course (Supplementary Fig. S7). In this setting, we did not observe adverse effects immediately after injection, and repeated dosing did not alter the pattern of metastasis we observed compared with those of other publications (42, 57). While we expect that *oatp1b3*-MRI with Gd-EOB-DTPA will be useful for tracking cancer cells and cancer-related cell populations, e.g., cellular immunotherapies, at the preclinical stage, the dose of the Gd(III) probe used here constrains clinical translation of this system.

In parallel, opportunities also exist to improve the imaging capabilities of *oatp1b3*-MRI with respect to both specificity and sensitivity. On the matter of whole-body imaging, the stomach and intestines exhibited high signal intensities on both precontrast and postcontrast T_1-weighted images, which may have obscured detection of small metastases at these sites; in addition, the small molecule probe Gd-EOB-DTPA does not readily cross the blood-brain barrier (BBB), hindering detection of brain metastasis until lesions grow enough to compromise BBB permeability. Although these issues can be addressed through fasting or additional steps that enable precontrast/postcontrast image subtraction and focused-ultrasound BBB opening, respectively, efforts are warranted to further optimize *oatp1b3*-MRI. Simply but effectively, incorporating a potato diet for 24 hours before imaging has been shown to practically eradicate nonspecific gastrointestinal T_1-weighted signals in mice and should therefore be implemented into all future *oatp1b3*-MRI animal protocols (58). In addition, development of next-generation Gd(III)-free paramagnetic probes targeting *oatp1b3* is underway, and small lipophilic molecules would be prime candidates to facilitate detection of brain metastasis on *oatp1b3*-MRI with the BBB intact (59, 60).

However, one remaining blind spot with little room for mitigation is the gallbladder, as it represents a collection site for *oatp1b3*-targeted probes that are categorically eliminated via the hepatobiliary pathway; however, we believe this represents a minor drawback in the context of the larger system. Finally, protein engineering provides opportunities to further improve system parameters and functionalize *oatp1b3* as a biosensor. For example, removal of the protein's downregulatory phosphorylation sites may increase the steady state concentration of OATP1B3 at the cell membrane for greater probe influx capacity; directed evolution can be employed to screen for mutants with more rapid probe-transport kinetics; and addition of sensory motifs can be conjugated to the channel to enable imaging of events like deep-brain neuronal activation. For now, however, *oatp1b3*-MRI offers a means to track *oatp1b3*-engineered cells in deep tissues of live animals over time with combined high resolution and high sensitivity. We anticipate that this platform will facilitate our abilities to cultivate clinically predictive preclinical models of metastasis (61), expand our understanding of the metastatic process, and provide a means to rigorously evaluate antimetastatic therapies *in vivo*.

Authors' Disclosures

J.A. Ronald reports grants from Canadian Institutes of Health Research during the conduct of the study. No disclosures were reported by the other authors.

Authors' Contributions

N.N. Nyström: Data curation, formal analysis, investigation, methodology, writing–original draft, writing–review and editing. **S.W. McRae:** Data curation, investigation, visualization. **F.M. Martinez:** Software, formal analysis, investigation, visualization, methodology. **J.J. Kelly:** Investigation, methodology. **T.J. Scholl:** Conceptualization, resources, data curation, supervision, funding acquisition, investigation, visualization, methodology, project administration, writing–review and editing. **J.A. Ronald:** Conceptualization, resources, data curation, supervision, funding acquisition, investigation, visualization, methodology, project administration, writing–review and editing.

Acknowledgments

Financial support for this manuscript was provided by Natural Sciences and Engineering Research Council of Canada (NSERC) Discovery Grants (RGPIN-2016-05420 to J.A. Ronald; RGPIN-2017-06338 to T.J. Scholl) and an Ontario Institute for Cancer Research Investigator Award (IA-028 to T.J. Scholl). N.N. Nyström is grateful to have received financial support from a Natural Sciences and Engineering Research Council of Canada Postgraduate Research Scholarship (2017–2021) and is an Amgen Awardee of the Life Sciences Research Foundation (2021–present). The authors would also like to acknowledge David Reese for providing helpful resources and the larger Cellular and Molecular Imaging Group at the Robarts Research Institute for insightful discussions. The authors would also like to acknowledge Karen Nygard and Reza Khazaee of the Biotron Facilities at the University of Western Ontario for their expertise on transmission electron microscopy, as well as Patrick Zakrzewski, Mohammed Farhoud, and Mat Brevard from EMIT Imaging Technologies for their expertise in cryo-fluorescence tomography.

The publication costs of this article were defrayed in part by the payment of publication fees. Therefore, and solely to indicate this fact, this article is hereby marked "advertisement" in accordance with 18 USC section 1734.

Note

Supplementary data for this article are available at Cancer Research Online (http://cancerres.aacrjournals.org/).

Received August 31, 2022; revised October 11, 2022; accepted December 7, 2022; published first December 13, 2022.

References

1. Lambert AW, Pattabiraman DR, Weinberg RA. Emerging biological principles of metastasis. Cell 2017;168:670–91.
2. Day CP, Merlino G, Van Dyke T. Preclinical mouse cancer models: a maze of opportunities and challenges. Cell 2015;163:39–53.
3. Gengenbacher N, Singhal M, Augustin HG. Preclinical mouse solid tumor models: status quo, challenges and perspectives. Nat Rev Cancer 2017;17: 751–65.
4. Francia G, Cruz-Munoz W, Man S, Xu P, Kerbel RS. Mouse models of advanced spontaneous metastasis for experimental therapeutics. Nat Rev Cancer 2011;11: 135–41.
5. Mezzanotte L, van 't Root M, Karatas H, Goun EA, Löwik CWGM. *In ivo* molecular bioluminescence imaging: new tools and applications. Trends Biotechnol 2017;35:640–52.
6. Giubellino A, Woldemichael GM, Sourbier C, Lizak MJ, Powers JF, Tischler AS, et al. Characterization of two mouse models of metastatic pheochromocytoma using bioluminescence imaging. Cancer Lett 2012;316:46–52.
7. Taus LJ, Flores RE, Seyfried TN. Quantification of metastatic load in a syngeneic murine model of metastasis. Cancer Lett 2017;405:56–62.
8. Kubota SI, Takahashi K, Nishida J, Morishita Y, Ehata S, Tainaka K, et al. Whole-body profiling of cancer metastasis with single-cell resolution. Cell Rep 2017;20: 236–50.
9. Pan C, Schoppe O, Parra-Damas A, Cai R, Todorov MI, Gondi G, et al. Deep learning reveals cancer metastasis and therapeutic antibody targeting in the entire body. Cell 2019;179:1661–76.
10. Entenberg D, Voiculescu S, Guo P, Borriello L, Wang Y, Karagiannis GS, et al. A permanent window for the murine lung enables high-resolution imaging of cancer metastasis. Nat Methods 2018;15:73–80.
11. Yan C, Brunson DC, Tang Q, Do D, Iftimia NA, Moore JC, et al. Visualizing engrafted human cancer and therapy responses in immunodeficient zebrafish. Cell 2019;177:1903–14.
12. Theruvath J, Menard M, Smith BAH, Linde MH, Coles GL, Dalton GN, et al. Anti-GD2 synergizes with CD47 blockade to mediate tumor eradication. Nat Med 2022.
13. Xia A, Yuan W, Wang Q, Xu J, Gu Y, Zhang L, et al. The cancer-testis lncRNA lnc-CTHCC promotes hepatocellular carcinogenesis by binding hnRNP K and activating YAP1 transcription. Nat Cancer 2022;3:203–18.
14. Krupnick AS, Tidwell VK, Engelbach JA, Alli VV, Nehorai A, You M, et al. Quantitative monitoring of mouse lung tumors by magnetic resonance imaging. Nat Protoc 2012;7:128–42.
15. Zhou Z, Qutaish M, Han Z, Schur RM, Liu Y, Wilson DL, et al. MRI detection of breast cancer micrometastases with a fibronectin-targeting contrast agent. Nat Commun 2015;6:7984.
16. Louie AY, Huber MM, Ahrens ET, Rothbacher U, Moats R, Jacobs RE, et al. *In vivo* visualization of gene expression using magnetic resonance imaging. Nat Biotechnol 2000;18:321–5.
17. Moore A, Josephson L, Bhorade RM, Basilion JP, Weissleder R. Human transferrin receptor gene as a marker gene for MR imaging. Radiology 2001; 221:244–50.
18. Cohen B, Dafni H, Meir G, Harmelin A, Neeman M. Ferritin as an endogenous MRI reporter for noninvasive imaging of gene expression in C6 glioma tumors. Neoplasia 2005;7:109–17.
19. Mukherjee A, Wu D, Davis HC, Shapiro MG. Noninvasive imaging using reporter genes altering cellular water permeability. Nat Commun 2016;7:13891.
20. Gilad AA, McMahon MT, Walczak P, Winnard PT Jr., Raman V, van Laarhoven HW, et al. Artificial reporter gene providing MRI contrast based on proton exchange. Nat Biotechnol 2007;25:217–9.
21. Shapiro MG, Ramirez RM, Sperling LJ, Sun G, Sun J, Pines A, et al. Genetically encoded reporters for hyperpolarized xenon magnetic resonance imaging. Nat Chem 2014;6:629–34.
22. Patrick PS, Kettunen MI, Tee SS, Rodrigues TB, Serrao E, Timm KN, et al. Detection of transgene expression using hyperpolarized 13C urea and diffusion-weighted magnetic resonance spectroscopy. Magn Reson Med 2015;73:1401–6.
23. Patrick PS, Hammersley J, Loizou L, Kettunen MI, Rodrigues TB, Hu DE, et al. Dual-modality gene reporter for in vivo imaging. Proc Natl Acad Sci USA 2014; 111:415–20.
24. Nystrom NN, Hamilton AM, Xia W, Liu S, Scholl TJ, Ronald JA. Longitudinal visualization of viable cancer cell intratumoral distribution in mouse models using Oatp1a1-enhanced magnetic resonance imaging. Invest Radiol 2019;54: 302–11.
25. Kelly JJ, Saee-Marand M, Nystrom NN, Evans MM, Chen Y, Martinez FM, et al. Safe harbor-targeted CRISPR-Cas9 homology-independent targeted integration for multimodality reporter gene-based cell tracking. Sci Adv 2021;7:eabc3791.
26. Iwano S, Sugiyama M, Hama H, Watakabe A, Hasegawa N, Kuchimaru T, et al. Single-cell bioluminescence imaging of deep tissue in freely moving animals. Science 2018;359:935–9.
27. Sellmyer MA, Richman SA, Lohith K, Hou C, Weng CC, Mach RH, et al. Imaging CAR T-cell trafficking with eDHFR as a PET reporter gene. Mol Ther 2020;28: 42–51.
28. Nyström NN, Yip LCM, Carson JJL, Scholl TJ, Ronald JA. Ronald development of a human photoacoustic imaging reporter gene using the clinical Dye indocyanine green. Radiol Imaging Cancer 2019;1:e190035.
29. Rydberg JN, Hammond CA, Huston J 3rd, Jack CR Jr, Grimm RC, Riederer SJ. T1-weighted MR imaging of the brain using a fast inversion recovery pulse sequence. J Magn Reson Imaging 1996;6:356–62.
30. Bydder GM, Young IR. MR imaging: clinical use of the inversion recovery sequence. J Comput Assist Tomogr 1985;9:659–75.
31. Yushkevich PA, Piven J, Hazlett HC, Smith RG, Ho S, Gee JC, et al. User-guided 3D active contour segmentation of anatomical structures: significantly improved efficiency and reliability. Neuroimage 2006;31:1116–28.
32. Chapy H, Klieber S, Brun P, Gerbal-Chaloin S, Boulenc X, Nicolas O. PBPK modeling of irbesartan: incorporation of hepatic uptake. Biopharm Drug Dispos 2015;36:491–506.
33. Powell J, Farasyn T, Kock K, Meng X, Pahwa S, Brouwer KL, et al. Novel mechanism of impaired function of organic anion-transporting polypeptide 1B3 in human hepatocytes: posttranslational regulation of OATP1B3 by protein kinase C activation. Drug Metab Dispos 2014;42:1964–70.
34. Gasteiger E, Gattiker A, Hoogland C, Ivanyi I, Appel RD, Bairoch A. ExPASy: The proteomics server for in-depth protein knowledge and analysis. Nucleic Acids Res 2003;31:3784–8.
35. Alam K, Crowe A, Wang X, Zhang P, Ding K, Li L, et al. Regulation of organic anion transporting polypeptides (OATP) 1B1- and OATP1B3-mediated transport: an updated review in the context of OATP-mediated drug-drug interactions. Int J Mol Sci 2018;19:855.
36. Jumper J, Evans R, Pritzel A, Green T, Figurnov M, Ronneberger O, et al. Highly accurate protein structure prediction with AlphaFold. Nature 2021; 596:583–9.
37. Huang H, Arighi CN, Ross KE, Ren J, Li G, Chen SC, et al. iPTMnet: an integrated resource for protein posttranslational modification network discovery. Nucleic Acids Res 2018;46:D542–D50.
38. York WS, Mazumder R, Ranzinger R, Edwards N, Kahsay R, Aoki-Kinoshita KF, et al. GlyGen: Computational and informatics resources for glycoscience. Glycobiology 2020;30:72–3.
39. Hornbeck PV, Kornhauser JM, Tkachev S, Zhang B, Skrzypek E, Murray B, et al. PhosphoSitePlus: a comprehensive resource for investigating the structure and function of experimentally determined posttranslational modifications in man and mouse. Nucleic Acids Res 2012;40:D261–70.
40. Miraux S, Massot P, Ribot EJ, Franconi JM, Thiaudiere E. 3D TrueFISP imaging of mouse brain at 4.7T and 9.4T. J Magn Reson Imaging 2008;28:497–503.
41. Szomolanyi P, Rohrer M, Frenzel T, Noebauer-Huhmann IM, Jost G, Endrikat J, et al. Comparison of the relaxivities of macrocyclic gadolinium-based contrast agents in human plasma at 1.5, 3, and 7 T, and blood at 3 T. Invest Radiol 2019;54: 559–64.
42. Puchalapalli M, Zeng X, Mu L, Anderson A, Hix Glickman L, Zhang M, et al. NSG mice provide a better spontaneous model of breast cancer metastasis than athymic (Nude) Mice. PLoS One 2016;11:e0163521.
43. Del Monte U. Does the cell number 10(9) still really fit one gram of tumor tissue? Cell Cycle 2009;8:505–6.
44. Richardson DS, Lichtman JW. Clarifying tissue clearing. Cell 2015;162:246–57.
45. Contag CH, Jenkins D, Contag PR, Negrin RS. Use of reporter genes for optical measurements of neoplastic disease *in vivo*. Neoplasia 2000;2:41–52.
46. Hung KE, Maricevich MA, Richard LG, Chen WY, Richardson MP, Kunin A, et al. Development of a mouse model for sporadic and metastatic colon tumors and its use in assessing drug treatment. Proc Natl Acad Sci USA 2010; 107:1565–70.
47. Anderson RL, Balasas T, Callaghan J, Coombes RC, Evans J, Hall JA, et al. A framework for the development of effective anti-metastatic agents. Nat Rev Clin Oncol 2019;16:185–204.

48. Martin OA, Anderson RL, Narayan K, MacManus MP. Does the mobilization of circulating tumor cells during cancer therapy cause metastasis? Nat Rev Clin Oncol 2017;14:32–44.
49. Obradovic MMS, Hamelin B, Manevski N, Couto JP, Sethi A, Coissieux MM, et al. Glucocorticoids promote breast cancer metastasis. Nature 2019;567: 540–4.
50. Obenauf AC, Zou Y, Ji AL, Vanharanta S, Shu W, Shi H, et al. Therapy-induced tumor secretomes promote resistance and tumor progression. Nature 2015;520: 368–72.
51. Tanaka Y, Araki K, Tanaka S, Miyagawa Y, Suzuki H, Kamide D, et al. Sentinel lymph Node-targeted therapy by oncolytic Sendai virus suppresses micrometastasis of head and neck squamous cell carcinoma in an orthotopic nude mouse model. Mol Cancer Ther 2019;18:1430–8.
52. Esposito M, Ganesan S, Kang Y. Emerging strategies for treating metastasis. Nat Cancer 2021;2:258–70.
53. Meirson T, Gil-Henn H, Samson AO. Invasion and metastasis: the elusive hallmark of cancer. Oncogene 2020;39:2024–6.
54. Kluger HM, Lev DC, Kluger Y, McCarthy MM, Kiriakova G, Camp RL, et al. Using a xenograft model of human breast cancer metastasis to find genes associated with clinically aggressive disease. Cancer Res 2005;65: 5578–87.
55. Kanda T, Ishii K, Kawaguchi H, Kitajima K, Takenaka D. High signal intensity in the dentate nucleus and globus pallidus on unenhanced T1-weighted MR images: relationship with increasing cumulative dose of a gadolinium-based contrast material. Radiology 2014;270:834–41.
56. McDonald RJ, McDonald JS, Kallmes DF, Jentoft ME, Paolini MA, Murray DL, et al. Gadolinium deposition in human brain tissues after contrast-enhanced MR imaging in adult patients without intracranial abnormalities. Radiology 2017; 285:546–54.
57. Jin X, Demere Z, Nair K, Ali A, Ferraro GB, Natoli T, et al. A metastasis map of human cancer cell lines. Nature 2020;588:331–6.
58. Kiryu S, Inoue Y, Yoshikawa K, Shimada M, Watanabe M, Ohtomo K. Diet and gastrointestinal signal on T1-weighted magnetic resonance imaging of mice. Magn Reson Imaging 2010;28:273–80.
59. Arvanitis CD, Ferraro GB, Jain RK. The blood-brain barrier and blood-tumor barrier in brain tumors and metastases. Nat Rev Cancer 2020;20:26–41.
60. Nystrom NN, Liu H, Martinez FM, Zhang XA, Scholl TJ, Ronald JA. Gadolinium-free magnetic resonance imaging of the liver via an Oatp1-targeted manganese(III) porphyrin. J Med Chem 2022.
61. Honkala A, Malhotra SV, Kummar S, Junttila MR. Harnessing the predictive power of preclinical models for oncology drug development. Nat Rev Drug Discov 2022;21:99–114.